Single and Triple Differential Cross Sections for Double Photoionization of H^-

F. L. Yip,[1] D. A. Horner,[2] C. W. McCurdy,[3,4] and T. N. Rescigno[4]

[1]*Department of Chemistry, University of California, Berkeley, CA 94720*
[2]*Los Alamos National Laboratory, Theoretical Division, Los Alamos NM 87545*
[3]*Departments of Applied Science and Chemistry, University of California, Davis, CA 95616*
[4]*Lawrence Berkeley National Laboratory, Chemical Sciences, Berkeley, CA 94720*

(Dated: February 15, 2007)

The hydride anion H^- would not be bound in the absence of electron correlation. Electron correlation drives the double photoionization process and, thus should impact double photoionization results most strongly for H^-. We present fully differential cross sections for the three-body breakup of H^- by single photon absorption. The absolute triple-differential and single-differential cross sections were yielded by *ab initio* calculations making use of exterior complex scaling within a discrete variable representation partial wave basis. Results calculated at photon energies of 18eV and 30eV are compared with reported cross sections for helium calculated at 20eV above the double ionization threshold. These comparisons show a clear signature of initial state correlation that differentiate the He and H^- cases.

I. INTRODUCTION

Recent experimental investigations have focused on double photoionization (DPI) of two-electron atoms [1–7] and molecules [8–11] as a sensitive probe of the correlated motion of electrons. The DPI problem is interesting from both experimental and theoretical viewpoints because the process by which an atom or molecule absorbs a photon of sufficient energy to eject two electrons into the continuum necessarily depends on electron correlation. Since the optical absorbtion is described by a sum of one-body dipole operators, any theoretical approach that treats the electrons in an independent particle model will produce inaccurate results for the amplitudes connecting the initial and final states. Such considerations have been previously addressed using different theoretical approaches for both atomic [12–25] and molecular [26–29] two-electron targets, with varying degrees of electron correlation being included in the initial and/or final states.

In addition to providing a fingerprint of correlated electronic motion, double photoionization problems represent an ambitious theoretical challenge because of the difficulty in applying the correct boundary conditions when two electrons enter the continuum. Since the pioneering theoretical work of the 1960s [30–32] to describe the correct asymptotic form of the wavefunction and the accompanying double ejection amplitude, numerous efforts have been applied to the more general three-body Coulomb breakup problem, including the use of anzatz wavefunctions [12–14], convergent close-coupling (CCC) methods [15–18], adapted R-matrix techniques [19, 20], time dependent close coupling (TDCC) methods [21–23], complex basis functions [24], and finally the method of exterior complex scaling (ECS) [25, 33, 34]. In addition to ensuring that the calculated wavefunctions maintain the proper boundary conditions for three-body breakup, each method requires a proper means to extract the physically relevant amplitude associated with the two-electron outgoing wave to produce cross sections that can be compared with experiment.

The canonical system for both double photoionization experimental investigations and theoretical calculations is the helium atom. This case represents a three-body Coulomb problem where electron repulsion represents a significant contribution to the energetics of the system. Theoretical treatments of helium DPI also benefit from atomic selection rules that restrict the overall final state produced from ground state ^1S helium to ^1P symmetry, thereby restricting the number of coupled angular momentum contributions that must be considered in any partial wave expansion of the total wavefunction.

Analogous to the helium case is double photoionization of the isoelectronic hydride anion H^-. Indeed, from a theoretical point of view, DPI of H^- is more interesting because of the greater importance of electron repulsion relative to the Coulomb attraction of the electrons to the nucleus when $Z = 1$. Thus, the atomic properties of H^- are more sensitive to electron correlation effects when compared to helium. This can be most easily demonstrated by simply comparing the results of a Hartree-Fock calculation of the He and H^- ground state energies. Whereas in the case of helium the ground state correlation energy is a few percent of the exact total energy, the Hartree-Fock energy of the hydride anion is above that of a 1s hydrogen atom and free electron by 0.33eV [35, 36]. The fact that an independent electron treatment yields increasingly more significant contributions to the exact energy of atoms as the nuclear charge Z increases indicates that the electron correlation effects should be most important in the prototypical case of H^-.

Numerous theoretical approaches have been applied to double photoionization of H^-, dating back to a multichannel J-matrix calculation by Broad and Reinhardt [37]. Since then, the problem has been treated by model calculations [38, 39], variationally [40], R-matrix methods [41], convergent close-coupling [42], time dependent close-coupling [43], and most recently by wavepacket propagation [44]. The application of these various methods have yielded absolute total cross sections for DPI of H^- as well as ratios of single ionization to double ioniza-

tion. However, the most detailed information concerning angular distributions and ejected electron energy sharing have yet to be reported. In this paper, we complete the picture by applying the method of exterior complex scaling to calculate the two-electron outgoing wavefunction and the associated scattering amplitudes in order to report triply-differential cross sections (TDCS) for H^-. We will demonstrate, using our converged calculations and comparisons between H^- and helium, that a clear signature of initial state correlation is revealed in the TDCS at extreme unequal energy sharing between the ejected photo-electrons, while near equal energy kinematics, the differences are far less prominent.

First, we present a brief overview of exterior complex scaling and describe its application to a partial wave decomposition of the outgoing wavefunction, highlighting the extraction of double photoionization amplitudes from the calculated solution. In Section III we present total cross sections of DPI of H^- and compare with previously reported calculated results. This is followed by singly- and triply-differential cross sections calculated at 18eV and 30eV photon energies, with our focus in the discussion being comparison of the present results with a similar treatment of the helium DPI case [25].

II. THEORETICAL FRAMEWORK

A. Exterior Complex Scaling Approach

The details of using exterior complex scaling (ECS) [45, 46] in theoretical treatments of problems involving two or more continuum electrons have been extensively discussed in a recent review [34]. The method has been successful in providing essentially exact results for both electron-impact ionization of atomic hydrogen [33] and double photoionization of atomic [25] and molecular two-electron targets [27–29]. Here we present the main broad strokes that illustrate how ECS successfully deals with problems invovling more than one continuum electron.

Exterior complex scaling avoids the difficulties associated with the explicit asymptotic form of multi-particle ejection wavefunctions mentioned above by imposing outgoing wave boundary conditions through a transformation of the radial coordinate of the ejected particles,

$$r \to \begin{cases} r, & r \le R_0 \\ R_0 + (r - R_0)e^{i\theta}, & r > R_0, \end{cases} \tag{1}$$

where R_0 defines a radius beyond which the coordinates of each electron become complex-scaled by a scaling angle θ. This rotation of r into the complex plane is illustrated in Figure 1, where the radial coordinate before R_0 corresponds to physical values. As previously discussed [34], this transformation avoids the difficulties associated with explcitly imposing proper boundary conditions by causing solutions with purely outgoing waves to decay exponentially along the complex-scaled contour. This is demonstrated in the lower panel of Fig. 1, which shows the exponential damping effect of complex scaling beyond $R_0 = 20$ on the one-dimensional outgoing wavefunction for a model problem [47]. Because of the sharp rotation of the radial coordinate into the complex plane at R_0, the wavefunction itself develops a discontinuous first derivative across this turning point. Several adapted techniques for describing the radial coordinate, including the use of finite elements [33], B-splines [47], and the discrete variable representation [48], have been employed to address the issues associated with exterior complex scaling. It is important to note that inside of R_0 the wavefunction corresponds to the physical solution, thus allowing the calculation of amplitudes aassociated with processes involving electron ejection, provided that the purely real part of the grid is large enough to allow the wavefunction to reach its asymptotic form. We briefly summarize the extraction of relevant DPI amplitudes calculated within the ECS framework in the following section.

B. Formulation of the Atomic Double Photoionization Problem

The double photoionization of a target atom by one photon is described by treating the absorbed radiation as a perturbation, yielding the so-called "first-order" driven-Schrödinger equation (in atomic units, here used throughtout),

$$\begin{aligned}(E_0 + \omega - H)|\Psi^+_{\rm sc}\rangle &= \epsilon \cdot \mu |\Psi_0\rangle \\ &= \left(\frac{d}{dz_1} + \frac{d}{dz_2}\right)|\Psi_0\rangle,\end{aligned} \tag{2}$$

where $\Psi^+_{\rm sc}$ is the purely outgoing wavefunction which includes double photoionization, Ψ_0 is the intial bound state of the target H^- atom with energy E_0, ϵ is the polarization direction of the photon defining the z-axis of the body-fixed frame and μ is the dipole operator, shown in Eq. 2 in the velocity gauge. With this choice of orientation, the final state for one-photon absobtion from a ^1S atom has the symmetry $^1P_0$. Thus, the selection rules assoicated with a dipole-allowed transition significantly reduce the number of angular momentum channels that must be considered, restricting the final state to include only $L = 1, M = 0$ contributions.

The atomic double photoionization amplitude $f(\mathbf{k}_1, \mathbf{k}_2)$ associated with $\Psi^+_{\rm sc}$ in an ECS apporach has been shown to be given, up to an irrelevant overall phase, by an integral over a finite volume within R_0 [49, 50],

$$f(\mathbf{k}_1, \mathbf{k}_2) = \left\langle \Phi^{(-)}_Z(\mathbf{k}_1, \mathbf{r}_1)\Phi^{(-)}_Z(\mathbf{k}_2, \mathbf{r}_2)\middle| E - T - V_1 \middle|\Psi^+_{\rm sc}\right\rangle, \tag{3}$$

where E is the total energy, T is the two-electron kinetic energy operator, and V_1 is the sum of all atomic nuclear attraction potentials,

$$V_1 = -Z/r_1 - Z/r_2\,. \tag{4}$$

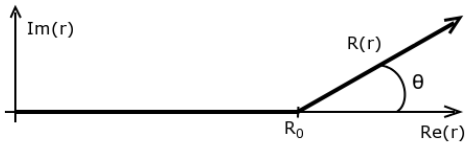

(a) ECS contour

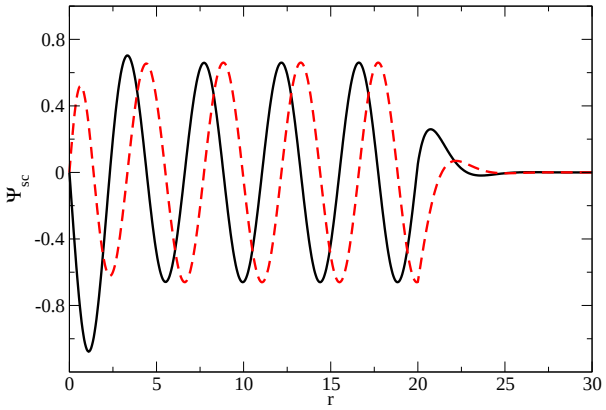

(b) Outgoing Waves under ECS

FIG. 1: (Color online) Exterior complex scaling in a single radial dimension. (a) ECS contour in the complex plane, demonstrating the rotation of the radial coordinate beyond R_0 into the upper-half complex plane by angle θ. (b) Real (solid line) and imaginary (dashed line) components of an outgoing wave solution for a model problem [47] along the ECS contour. The oscillatory nature of the outgoing waves is exponentially damped by the coordinate transformation beyond R_0. Inside of R_0 the outgoing wave is the physical solution.

The distorted wave "testing functions" $\Phi_Z^{(-)}(\mathbf{k}_1, \mathbf{r}_1)$ in Eq. 3 are momentum-normalized atomic Coulomb functions with charges Z equal to the charge of the nuclear potential in V_1 of Eq. 4, which is $Z = 1$ in the case of H^-. With that choice of effective nuclear charge on the testing functions, the finite-volume amplitude integral above projects out single-ionization contamination from the double-ionization channel by orthogonality of the Coulomb functions to the residual bound one-electron atom [34]. This choice for Z is in contrast to the usual "Peterkop condition" [32],

$$\frac{Z}{k_1} + \frac{Z}{k_2} = \frac{1}{k_1} + \frac{1}{k_2} - \frac{1}{\mathbf{k}_1 - \mathbf{k}_2}, \tag{5}$$

which is formally adopted to eliminate an overall volume-dependent phase. This phase, however, has been shown to have no effect on the calculated cross sections [51]. It must be stressed that the final state in Eq. 3 is *not* given by a product of Coulomb functions but is contained in the outgoing wave Ψ_{sc}^+; the Coulomb functions serve to extract the double ionization amplitude from all other energetically allowed processes (e. g. ,single ionization channels) contained in the exact solution.

The six-dimensional finite-volume integral of Equation 3 also leads to a further computational simplification by application of Green's theorem, thus allowing the amplitude to be computed as a surface integral. This allows the amplitude to be evaluated by considering only the asymptotic form of the scattered wave. The five-dimensional surface integral evaluated in hyperspherical coordinates is given by

$$f(\mathbf{k}_1, \mathbf{k}_2) = \int d\Omega_1 \int d\Omega_2 \int d\rho \int_0^{\pi/2} d\alpha \; \frac{\rho^5 \sin^2\alpha \cos^2\alpha}{2} \Phi^{(-)}(\mathbf{k}_1, \mathbf{r}_1)^* \Phi^{(-)}(\mathbf{k}_2, \mathbf{r}_2)^* \left[\frac{\overleftarrow{\partial}}{\partial\rho}\delta(\rho - \rho_0) - \delta(\rho - \rho_0)\frac{\overrightarrow{\partial}}{\partial\rho}\right] \Psi_{sc}^+(\mathbf{r}_1, \mathbf{r}_2), \tag{6}$$

where the arrows above the partial derivatives indicate the direction to which they operate and the delta functions enforce the evaluation of the amplitude along the hypersphere defined by $\rho = \sqrt{r_1^2 + r_2^2}$. The hyperangle α is defined by $\tan\alpha = r_2/r_1$, while Ω_1 and Ω_2 are the spherical polar angular coordinates of electrons 1 and 2, respectively.

The triple differential cross section describing the angular distributions of both ejected electrons and the energy sharing between them is given by

$$\frac{d^3\sigma}{dE_1 d\Omega_1 d\Omega_2} = \frac{4\pi^2}{\omega c} k_1 k_2 \left| f(\mathbf{k}_1, \mathbf{k}_2) \right|^2 . \tag{7}$$

C. Partial Wave Decomposition of Ψ_{sc}^+ and the Double Photoionization Amplitude

Following the prescription for practical calculation of the double photoionization amplitude utilized for both atomic helium [25] and molecular hydrogen [29], we seek to decompose the full scattered wave into angular components on a radial grid in order to implement exterior complex scaling. Thus, the scattered wave function that solves Eq. 2 is expanded as

$$\Psi_{sc}^+ = \sum_{l_1 m_1} \sum_{l_2 m_2} \frac{1}{r_1 r_2} \psi_{l_1 m_1, l_2 m_2}(r_1, r_2) Y_{l_1 m_1}(\hat{\mathbf{r}}_1) Y_{l_2 m_2}(\hat{\mathbf{r}}_2), \tag{8}$$

where unlike our earlier helium treatment, we have not explicitly partitioned the sum into direct and exchange components, but have instead summed over angular configurations (i. e. , lm-pairs) of the individual electrons. This sum, of course, is over lm-pair configurations that give an overall $L = 1, M = 0$ state required by photoabsorbtion selection rules. The two-dimensional radial function $\psi_{l_1 m_1, l_2 m_2}(r_1, r_2)$ multiplying the product

of spherical harmonics is represented in a product basis of 1D finite element-discrete variable representation (FEM-DVR) functions, similar to the approach used in molecular hydrogen DPI referenced above. The FEM-DVR radial basis is an attractive choice because of the computational efficiency gained as well as the natural complementarity for implementing exterior complex scaling [48].

The Coulomb functions in Equation 3 are similarly expanded in partial waves,

$$\Phi_Z^{(-)}(\mathbf{k},\mathbf{r}) = \left(\frac{2}{\pi}\right)^{1/2} \sum_{l,m} \frac{i^l e^{-i\eta_l}}{kr} \phi_{l,k}^{(c)}(r) Y_{lm}(\hat{\mathbf{r}}) Y_{lm}^*(\hat{\mathbf{k}}), \tag{9}$$

where $\phi_{l,k}^{(c)}(r)$ is a radial Coulomb function with asymptotic form

$$\phi_{l,k}^{(c)}(r) \to \sin(kr + (Z/k)\ln 2kr - l\pi/2 + \eta_l(k)), \tag{10}$$

as $r \to \infty$ and η_l represents the Coulomb phase

$$\eta_l(k) = \arg\Gamma(l+1-iZ/k), \tag{11}$$

with Z equal to the nuclear charge in the one-body potentials of Eq. 4, here $Z = 1$ for H^-.

By substituting the partial wave expansions of the full scattered solution $\Psi_{\rm sc}^+$ (Eq. 8) and the product of testing functions $\Phi_Z^{(-)}(\mathbf{k},\mathbf{r})$ (Eq. 9) into the expression for the full amplitude (Eq. 6) and integrating over the angular coordinates $d\Omega_1 d\Omega_2$ of both electrons, we arrive at an expression connecting the partial waves of $\Psi_{\rm sc}^+$ with the product of Coulomb waves,

$$f(\mathbf{k}_1,\mathbf{k}_2) = \sum_{l_1,m_1}\sum_{l_2,m_2} \left(\frac{2}{\pi}\right) i^{-(l_1+l_2)} e^{i\eta_{l_1}(k_1)+i\eta_{l_2}(k_2)} \times \Big[\mathcal{F}_{l_1,l_2,m_1,m_2}(k_1,k_2) Y_{l_1m_1}(\hat{\mathbf{k}}_1) Y_{l_2m_2}(\hat{\mathbf{k}}_2)\Big], \tag{12}$$

due to the orthogonality of the spherical harmonics. The sum is once again constrained to include only angular momentum pairs for which $M = m_1 + m_2 = 0$. Using the standard theory of rearrangement scattering, combined with a two-potential formalism, we can express the partial wave amplitudes $\mathcal{F}_{l_1,l_2,m_1,m_2}(k_1,k_2)$ appearing in Eq. 12 as [34]:

$$\begin{aligned}\mathcal{F}_{l_1,l_2,m_1,m_2}(k_1,k_2) &= \frac{1}{k_1k_2}\times \\ &\big\langle \phi_{l_1,k_1}^{(c)}(r_1)\phi_{l_2,k_2}^{(c)}(r_2)\big|E-h_1-h_2\big|\psi_{l_1m_1,l_2m_2}(r_1,r_2)\big\rangle \\ &= \frac{1}{k_1k_2}\int dr_1dr_2\phi_{l_1,k_1}^{(c)}(r_1)\phi_{l_2,k_2}^{(c)}(r_2)\times \\ &\qquad \big(E-h_1-h_2\big)\psi_{l_1m_1,l_2m_2}(r_1,r_2),\end{aligned} \tag{13}$$

where h_1 and h_2 are one-electron radial Hamiltonians,

$$h_i = -\frac{1}{2}\frac{d^2}{dr_i^2} + \frac{l(l+1)}{2r_i^2} - \frac{Z}{r_i}\,. \tag{14}$$

As before, the radial volume integral can be simplified by application of Green's theorem,

$$\begin{aligned}&\big\langle \phi^{(c)}{}_{l_1,k_1}(r_1)\phi_{l_2,k_2}^{(c)}(r_2)\big|E-h_1-h_2\big|\psi_{l_1m_1,l_2m_2}(r_1,r_2)\big\rangle = \\ &\quad\frac{\rho_0}{2}\int_0^{\pi/2}\Big[\phi_{l_1,k_1}^{(c)}(r_1)\phi_{l_2,k_2}^{(c)}(r_2)\frac{\partial}{\partial\rho}\psi_{l_1m_1,l_2m_2}(r_1,r_2) \\ &\quad-\psi_{l_1m_1,l_2m_2}(r_1,r_2)\frac{\partial}{\partial\rho}\phi_{l_1,k_1}^{(c)}(r_1)\phi_{l_2,k_2}^{(c)}(r_2)\Big],\Big|_{\rho=\rho_0} d\alpha,\end{aligned} \tag{15}$$

where ρ_0 defines the hypershere where the partial wave amplitudes are calculated, usually just inside of the ECS turning point R_0.

D. Cross Section Evaluation from Reduced Amplitudes

The partial wave amplitudes evaluated using Eqs. 13 and 15 are then returned to Eq. 12 to construct the full double photoionization amplitude $f(\mathbf{k}_1,\mathbf{k}_2)$. The TDCS can then be calcuated by Eq. 7.

The single differential cross section (SDCS), describing the energy sharing between both ejected electrons, is given by integrating the TDCS over all angles $d\Omega_1 d\Omega_2$ of electrons 1 and 2. Because of the orthonormality of the spherical harmonics, cross terms between reduced amplitudes for different angular configurations disappear, thus the SDCS is simply given by

$$\frac{d\sigma}{dE_1} = \frac{4\pi^2}{\omega c}k_1k_2\left(\frac{2}{\pi}\right)^2 \sum_{l_1m_1}\sum_{l_2m_2}\left|\mathcal{F}_{l_1,l_2,m_1,m_2}(k_1,k_2)\right|^2\,. \tag{16}$$

The total cross section for double photionization is then given by integrating the SDCS over the energy sharing range

$$\sigma = \int_0^E \frac{d\sigma}{dE_1}dE_1, \tag{17}$$

although the SDCS is sometimes defined to give the total cross section by integration over half energy range. Because the SDCS is symmetric about $E/2$, this simply redefines the SDCS as

$$\frac{d\widetilde{\sigma}}{dE_1} = 2\frac{d\sigma}{dE_1}, \tag{18}$$

thus also making the total DPI cross section

$$\sigma = \int_0^{E/2} \frac{d\widetilde{\sigma}}{dE_1}dE_1. \tag{19}$$

For consistency with our published SDCS results for helium, we have adopted the convention of Equation 19 in this work.

III. CALCULATED CROSS SECTIONS FOR DOUBLE PHOTOIONIZATION OF H^-

In order to solve the driven Schrödinger equation (Eq. 2) for the scattered wave, we must first describe the fully correlated ground state Ψ_0 in our FEM-DVR basis. This was accomplished by solving for the lowest eigenstate of the H^- Hamiltonian described on a grid with 15 Lobatto quadrature points within each of three finite elements chosen at $r = 5.0a_0$, $r = 10.0a_0$, and $r = 20.0a_0$. Such a large radial grid is required to describe the especially long exponential tail of the H^- ground state wave function. In addition, up to $l = 4$ was used to describe the ^1S state, yielding a ground state energy of -0.52768 hartrees. The exact ground state energy of H^- is -0.52775 a. u. [52], indicating that electron correlation is well accounted for in our ground state wave function expansion.

A. Convergence Tests

The final state ^1P continuum of Ψ^+_{sc} from which the following cross sections were calculated was expanded according to Eq. 8 on a radial grid with 15th-order DVR points in several finite elements with an ECS turning point at $R_0 = 100$ bohr. This large grid size is more consistent with those used in atomic hydrogen electron-impact ionization problems. It follows that a larger grid is required to fully capture the dynamics involved in DPI when the nuclear attraction potential diminshes in mangnitude in going from $Z = 2$ to $Z = 1$. This observation was discussed in the B-spline treatment of DPI from helium [25] and in the FEM-DVR calculation of molecular hydrogen DPI [29], where smaller radial grids were sufficient to produce converged results.

Figure 2 demonstrates the convergence of the calculated results with respect to several parameters. The triple differential cross sections were calculated for an 18eV photon with the fixed electron leaving at an angle $\theta_1 = 40°$ and with 80% of the available excess energy. A comparison of the cross sections calculated in the length and velocity gauges is shown in Fig. 2(a). The differences between calculations taken in the length and velocity gauges are graphically indistinguishable in these TDCS plots. Therefore the other TDCS results in Fig. 2 and in the examples throughout this work. unless otherwise stated, are shown only in the velocity gauge.

Figure 2(b) demonstrates the convergence of the calculated results with increasing partial waves. The results shown were computed using a value of $l = 4$ for the initial state Ψ_0 and the various maximum l values shown to describe the final state Ψ^+_{sc}. Increasing the number of partial waves in the initial state to $l = 5$ showed no changes from these results, indicating an accurate description of the ground state wave function was used. The general trend of the TDCS is given by the $l = 4$ results with the most significant change occuring by including up to $l = 6$ partial waves. The results for maximum $l = 8$ and $l = 10$ are nearly identical, indicating that inclusion of partial waves of up to $l = 8$ yields converged results.

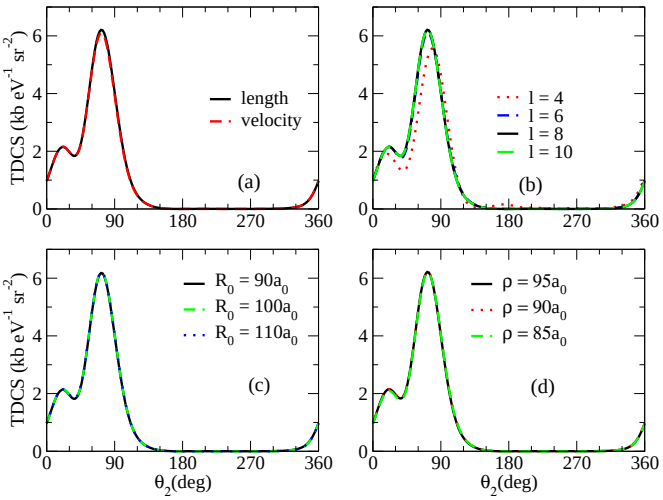

FIG. 2: (Color online) Convergence tests for the H^- TDCS, calculated at 18eV photon energy with the first electron direction fixed at $\theta_1 = 40°$ and carrying 80% of the excess energy. (a) TDCS results calculated in both length and velocity gauge. (b) Convergence of velocity-gauge results as more partial wave terms are included. (c) Convergence with respect to the radial grid, varying the extent of the complex scaling point R_0. (d) Convergence of the TDCS with different hyperspherical radii ρ for evaluation of the finite-volume amplitude calculations.

It should be noted that the number of partial waves necessary to give converged results for H^- is significantly larger than the maximum value of l used to treat double photoionization in helium [25]. The electron-electron repulsion term $1/|r_1 - r_2|$, which is treated by a multipole expansion, is more dominant for H^- than for any other two-electron atom. Thus, the accuracy of the computed results depends more sensitively on the number of partial waves taken for H^- compared to helium, requiring higher l terms to converge the calculation as electron repulsion becomes more significant.

In addition to the angular decomposition, convereged results must be robust with respect to the radial component parameters. The variation of the computed TDCS with radial grid extent is shown in Fig. 2(c). The exterior complex scaling point R_0 was placed at 90, 100 and 110 bohr. The results are insensitive to this change, further indicating that our radial basis is essentially complete and that the calculation is converged.

Finally, to ensure that the radial grid is sufficient to extract accurate double photoionization amplitudes by means of the finite volume integral of Eq. 3, Fig. 2(d) shows TDCS results calcuated at different extraction radii ρ just before the ECS turning point $R_0 = 100a_0$. The physically meaningful DPI amplitude should be insensitive to the finite volume used to extract it from the

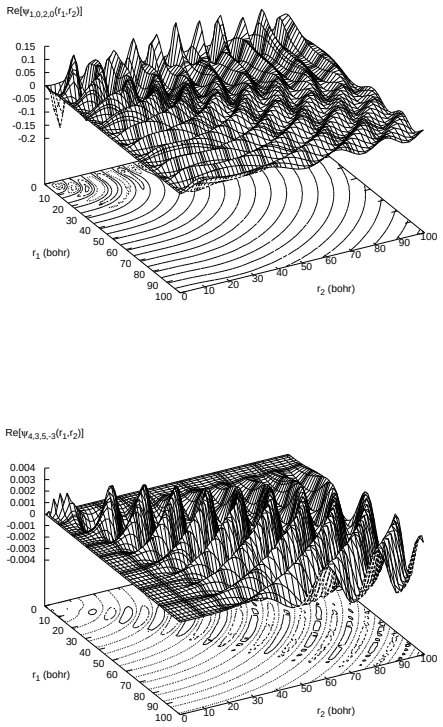

FIG. 3: Real component of two partial waves, labeled by the angular momentum of each electron (l_1, m_1, l_2, m_2), contributing to the full scattered wavefunction. The upper panel corresponds to the angular contribution $(1, 0, 2, 0)$. The lower panel shows the partial wave for $(4, 3, 5, -3)$. Peaks along the r_1 or r_2 axis correspond to amplitude in single-ionization channels.

outgoing scattered wave, provided that such a finite volume is large enough to fully account for the dynamics of the problem. Fig. 2(d) illustrates that that is the case.

With these issues of convergence now resolved, we now examine the components of the outgoing scattered wave that make up the full solution. Such an exercise reveals interesting aspects about the partial-wave contributions to double photoionization as well as the competing single photoejection process. Figure 3 displays the real part of two contributing partial waves of the full solution $\Psi^+_{\rm sc}$ along the real radial grid. The upper panel shows $\mathrm{Re}\{\psi_{l_1 m_1, l_2 m_2}\}$ for a low angular momentum pair $l_1 = 1, m_1 = 0, l_2 = 2, m_2 = 0$. The contributions of this partial wave to single ionization are evident by the large peaks near the r_2 axis where r_1 is small. The relative magnitude of the higher angular momentum partial wave shown in the lower panel is much smaller, but displays a significant contribution to the double photoionization channel. The significance of the high partial-wave components confirms the importance of electron correlation in describing the double photoionization process.

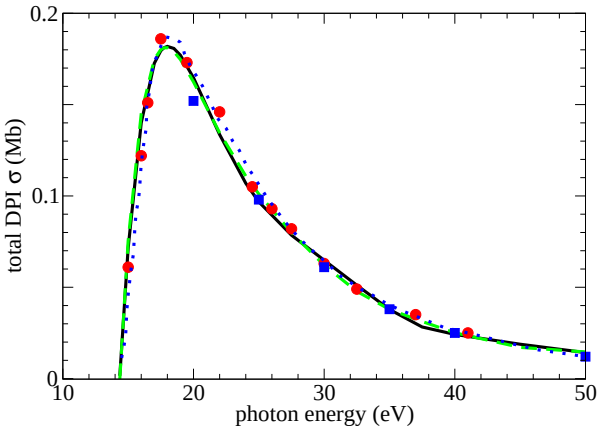

FIG. 4: (Color online) Total double photoionization cross section of H^- at various energies. The solid curve and dashed curve correspond to the present results calculated in the length and velocity gagues, respectively. Circles correspond to results calculated through wavepacket propagation by Foumouo *et al.* [44]. Squares correspond to results reported by Pindzola and Robicheaux calculated using TDCC methods [43]. Dotted curve corresponds to results in the velocity guage reported by Kheifets and Bray calculated using CCC methods [42]

B. Total Double Photoionization Cross Section

Previously published theoretical calculations treating double photoionization of H^- have only presented total DPI cross sections. To compare with some of these results, we calculated the total DPI cross section at several energies according to Eq. 19. The results are presented in Figure 4. The results calculated in both the length and velocity gauges are nearly identical and agree well with the results calculated by wavepacket propagation [44], by time-dependent close coulpling [43]and by convergent close coupling in the velocity gauge [42] (circles, squares and diamonds in Fig. 4, respectively). In addition, we calculated the ratio of single-to-double photoionization at several energies. The single ionization cross sections were obtained by subtracting the calculated total DPI cross section from the total photoabsorbtion cross section obtained from the optical theorem. Calculation of the single-to-double ratios yielded results in good agreement with those published by both Meyer, Greene and Esry [41] and Pindzola and Robicheaux [43].

Some interesting things to note about the DPI cross section of H^- include its rather large magnitude compared to helium, consistent with its small, correlation-induced binding energy. The double-to-single photoionization cross section ratio peaks at $\sim 3.7\%$ for helium, while for H^- the peak ratio is substantially larger, near 10%. In addition, the location of the maximum for H^- is only a few eV above its threshold, whereas the max-

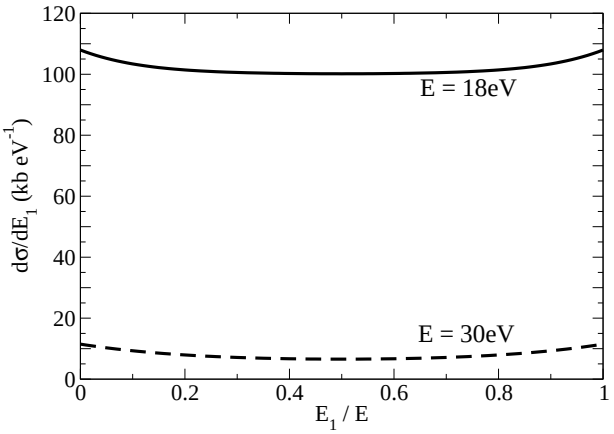

FIG. 5: Single differential cross section for DPI of H^- at two photon energies, 18eV (solid curve) and 30eV (dashed curve), plotted against the percentage of energy carried by the first electron. The product of half the area under each curve and the excess energy above the double ionization threshold yields the integral DPI cross section.

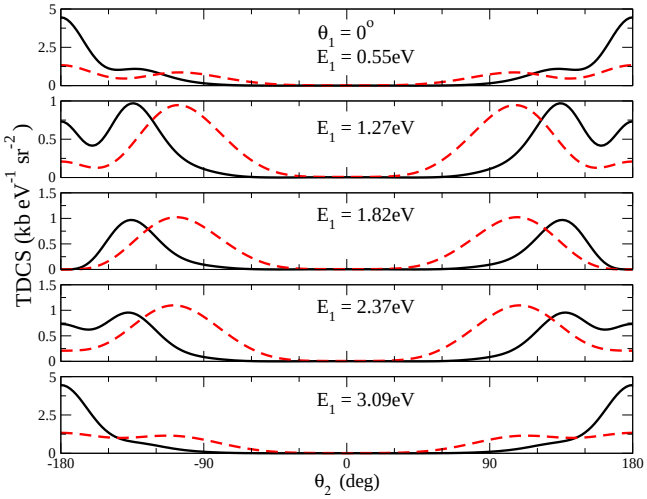

FIG. 6: (Color online) TDCS for double photoionization of H^- with a photon 3.64eV above threshold (solid line) and of helium (dashed line) with a photon 20eV above threshold, with θ_1 fixed at 0° at various energy sharings. Selection rules [13] prevent the second electron from exiting opposite the first in the center panel. As the symmetry is broken, this quickly becomes the preferred direction. The results for helium are scaled by a factor of 100.

imum total cross section for helium lies $\sim$ 20eV above the DPI threshold. However, the ratio of excess energy to the double ionization potential at these maxima are nearly the same.

C. Single Differential Cross Sections at 18 and 30eV

The single differential cross section results for photon energies 18eV and 30eV are shown in Fig. 5. At $\omega = 18$eV, representing the maximum integral DPI cross section, the SDCS for H^- is two orders of magnitude larger than the size of the largest SDCS for helium and quickly diminishes in magnitude as the photon energy is increased. The general variation of the SDCS as the energy shared between the electrons changes, however, appears like those exhibited in helium and molecular hydrogen. In all these cases, the SDCS feature a similar trend as shown in Fig. 5, with a relatively flat curve that increases by only a few percent as the energy sharing becomes more unequal.

D. Triple Differential Cross Sections at 18 and 30eV

The most detailed information that can be observed in a double photoionization experiment is the triple differential cross section. We begin by considering the variation of the cross section with energy sharing. Figure 6 shows computed TDCS results for an 18eV photon (3.64eV above threshold) with $\theta_1 = 0°$, i. e. , with the first electron ejected along the polarization axis. The panels feature cases of energy sharings, from top to bottom, of 15%, 35%, 50%, 65%, and 85% for the first electron. Included in Fig. 6 are the corresponding TDCS results for DPI of helium calculated at peak energy (20eV above threshold). The magnitude of helium cross sections has been scaled by a factor of 100. As the energy sharing is varied from the equal-sharing case, the cross section increases towards the direction opposite the first electron, similar to the case for helium. However, the H^- case shows a much more rapid approach to the opposite direction of ejection at less unequal energy sharings than does helium. The general shape of TDCS for helium at 15% and 85% energy sharing thus agree more with the TDCS corrsponding to 35% and 65% energy sharings, respectively, in the case of H^-. In addition, the more extreme unequal energy sharing cases for H^- show a larger variation in the magnitude of the cross sections relative to equal energy sharing than does the helium case.

Figure 7 shows H^- TDCS results for various equal energy sharing orientations at 18eV photon energy. In general, the peaks are more pronounced for H^- when compared to similar cases of DPI of helium at 20eV above threshold, also shown in Fig. 7, but the overall trends within each panel and variation as the orientation of the first outgoing electron changes are similar to helium. The location of the peaks in θ_2 are slightly further away from the fixed ejected electron's direction in H^- compared to the corresponding peak angles found in helium. This seems reasonable given the more significant contribution electron repulsion accounts for in H^- than in helium.

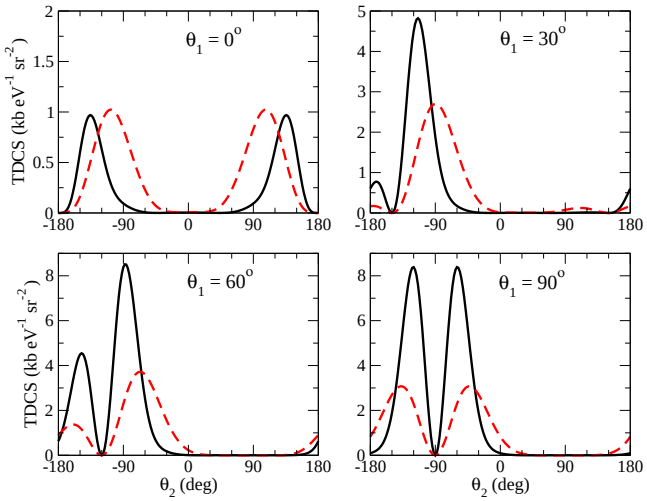

FIG. 7: (Color online) TDCS of H^- for a photon 3.64eV above threshold (solid curve) with various fixed first electron angles θ_1 and equal energy sharing. The dashed curves are similar cases involving DPI of helium at 20eV above threshold, scaled by a factor of 100. Selection rules cause the cross section to disappear opposite θ_1.

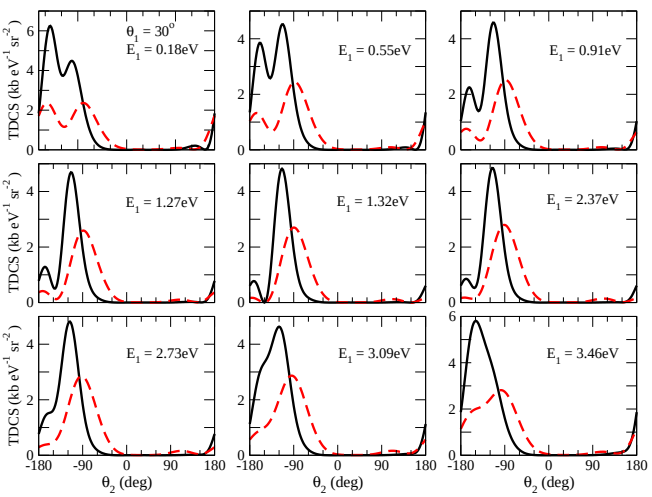

FIG. 8: (Color online) H^- double photoionization TDCS for a photon 3.64eV above threshold (solid curve) with fixed first electron angle $\theta_1 = 30°$ at various energy sharings. Also shown are corresponding TDCS results for DPI of helium at 20eV above threshold (dashed curve) scaled by a factor of 100. The panels correspond to 5%, 15%, 25%, 35%, 50%, 65%, 75%, 85%, and 95% available energy carried by the first electron.

Again, the magnitude of the TDCS variation changes more dramatically for H^- than for helium as the first electron orientation is varied. The TDCS relative magnitude changes are two to three times larger in H^- than the variations observed for helium. Similarly evident from the panels in Fig. 7 as in the helium case is the selection rule that prevents the two electrons from exiting in opposite directions at equal energy sharing [13].

Figure 8 displays TDCS results for a fixed electron at $\theta_1 = 30°$ at various energy sharings for both H^- and helium at peak double photoionization energies. Again, similar trends exist between these examples for H^- and helium as the energy sharing is varied, the most pronounced differences between the two cases occring when one electron moves away much faster than the other. The angles of the maximum cross section again vary further away from the first electron compared to helium as mention above.

The TDCS results for different orientations ($\theta_1 = 60°$ and $\theta_1 = 90°$) with unequal energy sharing ($E_1 = 15\%$ and $E_1 = 85\%$ of 3.64eV above threshold) are shown in Figure 9. The general features of the cross sections appear similar to the corresponding cases for helium DPI at peak photon energy, shown as the dashed line in Fig. 9.

To better visualize the double ionization beyond the coplanar geometry, i. e. , with both electrons exiting in the same plane as the polarization, three-dimensional TDCS results of DPI from H^- at 3.64eV above threshold are shown in the upper panel of Figure 10. The lower panel displays a corresponding TDCS calculated for helium DPI by a photon with 20eV above threshold energy. The first electron in both cases is fixed at $\theta_1 = 30°$ with equal energy sharing. Again, the selection rule preventing the second electron from being ejected opposite θ_1 is demonstrated, causing a flattening out of the larger lobe near $\theta_2 = 210°$. More prominent than in the helium case is the small lobe near $\theta_2 = 180°$. The case of unequal energy sharing is illustrated in the two panels of Figure 11, where the upper panel displays the H^- three-dimensional TDCS with the first electron carrying away 15% of the available energy and the lower panel displays similar results calculated for helium. The non-applicability of the equal energy sharing selection rule is most apparent for both cases. The length of the arrows for the H^- results shown in the upper panels of Figs. 10 and 11 correspond to 1600 barns per eV per unit solid angle, while for the helium cases of the lower panels the arrow lengths correspond to 20 barns per eV per steradian. The H^- cross sections of Figs. 10 and 11 exhibit a magnitude several orders larger than for helium, but perhaps most striking is the orientation of the larger lobe away from the xy-plane for H^-. The helium case shows a preferred ejection into the xy-plane away from the first electron. The different orientations of the major lobes for H^- and helium is illustrated more dramatically in three dimensions.

One of the influences on the features of the triple differential cross sections is the energy above threshold available to both electrons. Foster and Colgan [53] report calculated TDCS results that show comparable angluar features for cases in which the ratio of excess energy available to the ejected electrons to the corresponding double ionization potential is similar for two-electron atoms with $Z \geq 2$. The cross sections calculated above for H^- have

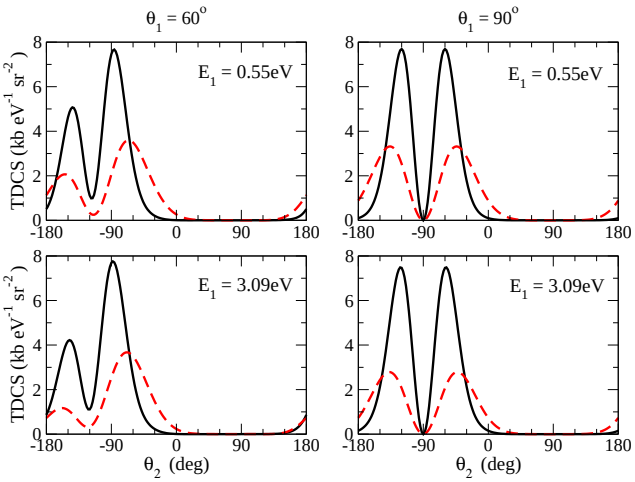

FIG. 9: (Color online) TDCS of double photoionization of H^- for a photon 3.64eV above threshold (solid curve) and helium for a photon 20eV above threshold (dashed curve) with fixed first electron angles $\theta_1 = 60°$ (first column) $\theta_1 = 90°$ (second column) and at energy sharings of 15% (first row) and 85% (second row) available energy carried by the first electron. The helium results have been scaled by a factor of 100.

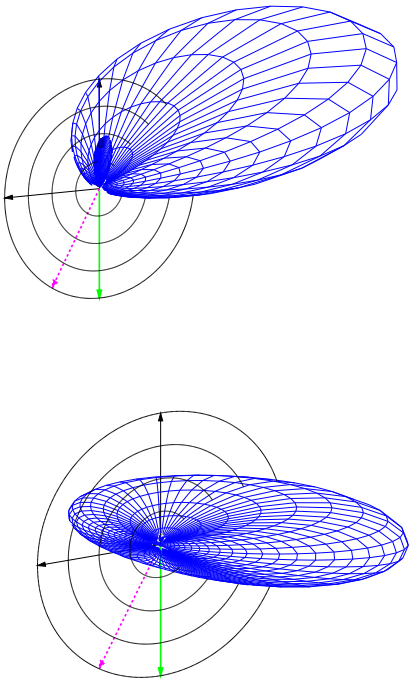

FIG. 10: (Color online) Three-dimensional TDCS results for DPI of H^- with a photon 3.64eV above threshold (upper panel) and for helium with a photon 20eV above threshold (lower panel) with equal energy sharing and the first electron ejected in a direction fixed at $\theta_1 = 30°$ (shown as dashed arrow) from the polarization direction (solid arrow). The direction of the larger lobe is further away from the fixed direction θ_1 in H^- than observed for helium. The arrow lenghts of the H^- panel are 80 times larger than those shown in the lower panel helium case.

been calculated at an energy where the total DPI cross section is maximal, lying at an energy close to the double ionization threshold. Because the general features may be strongly influenced by threshold effects, we now consider the TDCS results calculated for double photoionization with a photon of 30eV, 15.64eV above the H^- double ionization threshold. This photon energy corresponds to total ejection energies closer to those for which TDCS results for helium have been measured experimentally and theoretically calculated.

Figure 12 shows TDCS calculated for H^- at 30eV photon energy with equal energy sharing at various ejected electron angles. Comparing these results and those calculated for H^- at 18eV (Fig. 7) with results calculated at 20eV above threshold for helium (shown as the dashed line in Fig. 12) demonstrates that there are more similarities between H^- and helium at more comparable above-threshold energies for equal energy sharing. The results of Fig. 12 demonstrate that the cross section peaks as a function of θ_2 at angles more similar to helium at this higher photon energy. Furthermore, the relative magnitude of the cross section features both within each panel and among the different angles for θ_1 are closer to those exhibited in helium than the nearer-to-threshold case shown in Fig. 7.

The case of unequal energy sharing at 30eV photon energy and fixed angle for one ejected electron is illustrated in Fig. 13. The results in general show as much variation as those in Fig. 8 when compared to helium DPI at 20eV above threshold. Consistent with the results mentioned above, better agreement between the general shape and relative peak heights compared to helium occurs for the 30eV photon near equal energy sharing. The larger differences occur at more severe energy sharings.

Figure 14 highlights the changes that occur as the electrons have more available kinetic energy when the photon energy is changed from 18eV to 30eV. The TDCS results calculated for various geometries and energy sharings at 30eV scaled by a factor of 16 (solid curve) are shown along with the results calculated with an 18eV photon from Fig 9 (dashed curve). Also shown are the corresponding helium TDCS results calculated at photon energy 20eV above the DPI threshold (dash-dotted curve). The overall trends are similar, however with the H^- cross section maxima located at angles closer to those in helium for the 30eV photon.

Finally, to compare with Figures 10 and 11 we present in Fig. 13 a three-dimensional view of the TDCS calculated at 30eV photon energy with θ_1 fixed at 30°. The op left panel shows the case of equal energy sharing for H^-, followed by the corresponding helium case at photon energy 20eV above threshold shown in the top right panel. The overall shape of the cross section and orienta-

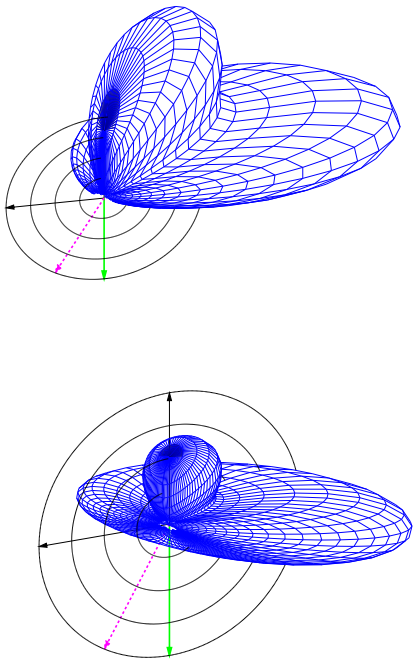

FIG. 11: (Color online) Three-dimensional TDCS results for DPI of H^- involving a photon 3.64eV above threshold (upper panel) and for helium with a photon 20eV above threshold (lower panel) with 15% energy sharing carried by the first electron into fixed direction $\theta_1 = 30^\circ$ (shown as dashed arrow) from the polarization direction (solid arrow). The breakdown of the selection rule manifest in Fig. 10 is apparent. The arrow lenghts of the H^- panel are 80 times larger than those shown in the lower panel helium case.

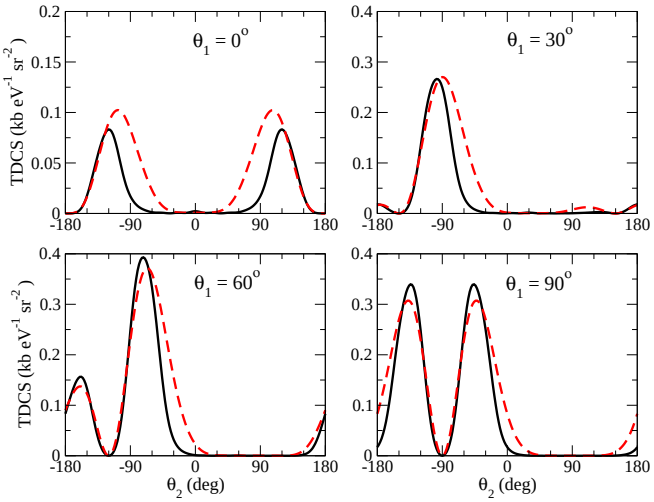

FIG. 12: (Color online) TDCS for double photoionization of H^- (solid curve) involving a 30eV photon (15.64eV above threshold) at various fixed first electron angles θ_1 and equal energy sharing. Also reproduced are the corresponding helium results (dashed curve) shown in Fig. 7, now scaled by a factor of 10.

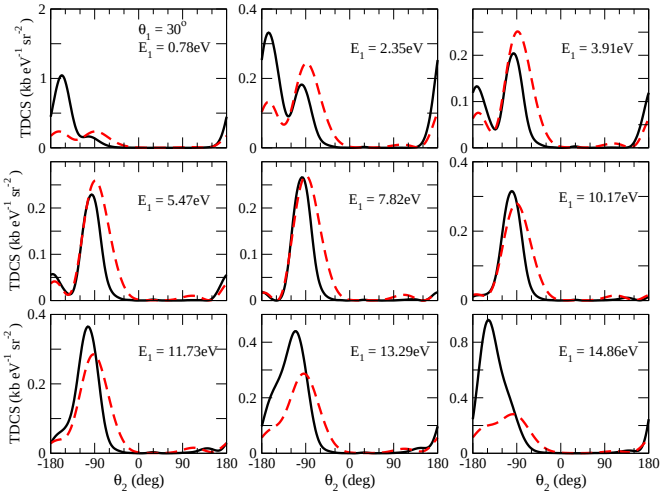

FIG. 13: (Color online) TDCS for a 30eV photon (solid curve), 15.64eV above the H^- DPI threshold the, with fixed first electron angle $\theta_1 = 30^\circ$ and various energy sharings. Also shown are the corresponding helium TDCS results dislayed in Fig. 8 (dahsed curve), though now scaled by a factor of 10. The panels correspond to 5%, 15%, 25%, 35%, 50%, 65%, 75%, 85%, and 95% available energy carried by the first electron.

tion along the xy-plane is more similar to the results for DPI of helium than was the case for H^- shown in Fig. 10 involving an 18eV photon. The smaller lobe opposite the larger one about the selection-rule prohibited direction in Fig. 10 is more suppressed in the more comparable excess energy case of Fig. 15. The bottom left panel displays the case where the first electron carries away 15% of the 15.64eV above threshold energy. In this case the cross section becomes significant in the lobe outside of the xy-plane. Here, the TDCS for H^- is significantly less like the unequal energy sharing case of helium, reproduced in the bottom right panel, as demonstrated in the extreme energy sharing cases shown in Fig. 13. The scale of the H^- cross sections in Fig. 15 is ten times smaller than the H^- TDCS displayed in Figs. 10 and 11.

IV. CONCLUSIONS

The triple-differential cross sections, representing the most detailed information measurable for atomic double photoionization processes, have been presented for the H^- negative ion, along with SDCS and total cross section results. The H^- system presents a challenging case to treat theoretically because of the significant contribution of electron correlation to the overall dynamics, more so than for any other atomic three-body problem.

Results calculated for H^- show general trends similar to those theoretically calculated and experimentally observed in helium double photoionization, where nuclear attraction is comparatively more dominant. Significant

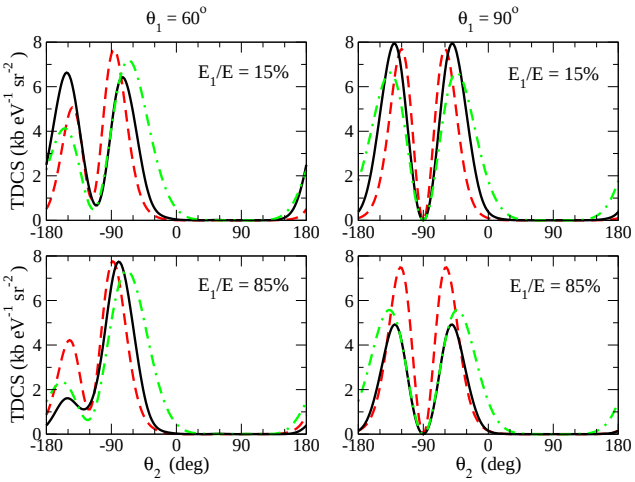

FIG. 14: (Color online) TDCS for double photoionization of H^- involving a 30eV photon (solid curve) and an 18eV photon (dashed curve) and for DPI of helium involving a 99eV photon (dash-dotted curve) with fixed first electron angles $\theta_1 = 60^\circ$ (first column) $\theta_1 = 90^\circ$ (second column) and at energy sharings of 15% (first row) and 85% (second row) available energy carried by the first electron. The solid curve results have been scaled by a factor of 16 while the helium results have been scaled by a factor of 200.

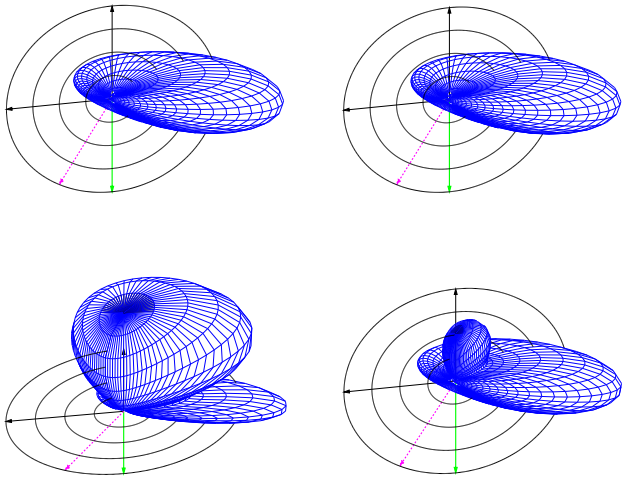

FIG. 15: (Color online) Top left panel: three-dimensional H^- TDCS results for a 30eV photon with equal energy sharing. Top right panel : corresponding case for helium at 99eV photon energy. Bottom left panel: H^- TDCS with 15% energy sharing. Bottom right panel: unequal energy sharing results for helium DPI. The direction of the first ejected electron is fixed at $\theta_1 = 30^\circ$ (shown as dashed arrow) from the polarization direction (solid arrow). The scale of the arrow lengths for the helium panels is the same as those for helium results depicted in Figs. 10 and 11, while the scale of the H^- panels is 8 times greater than the helium examples depicted.

differences between these two atomic cases however exist, most notably in the results presented at 18eV where the total cross section is maximal. The location of this maximum near the H^- double ionization threshold produces effects different from those observed for DPI of helium at its maximum total cross section 20eV above threshold. When the photon energy is increased to 30eV to provide more comparable ejection energies above threshold, the differences between the H^- and helium TDCS results appear less severe. This trend is more the case for equal energy sharing, with significant differences remaining in the extreme unequal energy sharing cases. These extremes with one electron moving much more slowly than the other would appear to be more sensitive to electron correlation effects in H^- than in helium where nuclear attraction is more significant. For extreme asymmetric energy sharing, one expects post-collision interaction effects to be relatively less important, so it is not surprising that these cases reflect the significant differences in initial state correlation between H^- and helium.

Acknowledgments

This work was performed under the auspices of the US Department of Energy by the University of California Lawrence Berkeley National Laboratory under Contract DE-AC02-05CH11231 and was supported by the U.S. DOE Office of Basic Energy Sciences, Division of Chemical Sciences.

[1] R. Wehlitz, F. Heiser, O. Hemmers, B. Langer, A. Menzel, and U. Becker, Phys. Rev. Lett. **67**, 3764 (1991).
[2] M. Braüning, R. Dörner, C. L. Cocke, M. H. Prior, B. Kriässig, A. S. Kheifets, I. Bray, A. Braüning-Demian, K. Carnes, S. Dreuil, et al., J. Phys. B **31**, 5149 (1998).
[3] V. Mergel, M. Achler, R. Dörner, K. Khayyat, T. Kambara, Y. Awaya, B. Nyström, L. Spielberger, J. H. McGuire, J. Feagin, et al., Phys. Rev. Lett. **80**, 5301 (1998).
[4] J. A. R. Samson, W. C. Stolte, Z. X. He, J. N. Cutler, Y. Lu, and R. J. Bartlett, Phys. Rev. A **57**, 1906 (1998).
[5] J. P. Weightman, S. Cvejanović, and T. J. Reddish, J. Phys. B **31**, 1753 (1998).
[6] K. Soejima, A. Danjo, K. Okuno, and A. Yagishita, Phys. Rev. Lett. **83**, 1546 (1999).
[7] A. Huetz and J. Mazeau, Phys. Rev. Lett. **85**, 530 (2000).
[8] T. Weber, A. O. Czasch, O. Jagutzki, A. K. Müller, V. Mergel, A. Kheifets, E. Rotenberg, G. Meigs, M. H. Prior, S. Daveau, et al., Nature **431**, 437 (2004).
[9] T. Weber, A. Czasch, . Jagutzki, A. Müller, V. Mergel, A. Kheifets, J. Feagin, E. Rotenberg, G. Meigs, M. H. Prior, et al., Phys. Rev. Lett. **92**, 163001 (2004).
[10] T. Weber, Ph.D. thesis, Institut fuer Kernphysik, Frankfurt (2003), available at `http://hsb.uni-frankfurt.de/web/publications/diplom_doktor/`.
[11] M. Gisselbrecht, M. Lavollée, A. Huetz, P. Bolognesi, L. Avaldi, D. P. Seccombe, and T. J. Reddish, Phys. Rev. Lett. **96**, 153002 (2006).
[12] M. Brauner, J. S. Briggs, and H. Klar, J. Phys. B **22**, 2265 (1989).
[13] F. Maulbetsch and J. S. Briggs, J. Phys. B **26**, 1679 (1993).
[14] J. Berakdar and J. S. Briggs, Phys. Rev. Lett. **72**, 3799 (1994).
[15] I. Bray and A. T. Stelbovics, Phys. Rev. A **46**, 6995 (1992).
[16] I. Bray and D. V. Fursa, Phys. Rev. A **54**, 2991 (1996).
[17] I. Bray, Phys. Rev. Lett. **78**, 4721 (1997).
[18] A. Kheifets and I. Bray, J. Phys. B **31**, L447 (1998).
[19] P. Selles, L. Malegat, and A. K. Kazansky, Phys. Rev. A **65**, 032711 (2002).
[20] P. J. Marchalant and K. Barschat, Phys. Rev. A **56**, R1697 (1997).
[21] F. Robicheaux, M. S. Pindzola, and D. R. Plante, Phys. Rev. A **55**, 3573 (1997).
[22] J. Colgan and M. S. Pindzola, J. Phys. B **34**, L457 (2001).
[23] J. Colgan and M. S. Pindzola, Phys. Rev. A **65**, 032729 (2002).
[24] M. Pont and R. Shakeshaft, Phys. Rev. A **51**, 494 (1995).
[25] C. W. McCurdy, D. A. Horner, T. N. Rescigno, and F. Martín, Phys. Rev. A **69**, 032707 (2004).
[26] J. Colgan, M. S. Pindzola, and F. Robicheaux, J. Phys. B. **37**, L377 (2004).
[27] W. Vanroose, F. Martín, T. N. Rescigno, and C. W. McCurdy, Phys. Rev. A **70**, 050703 (2004).
[28] W. Vanroose, F. Martín, T. N. Rescigno, and C. W. McCurdy, Science **310**, 1787 (2005).
[29] W. Vanroose, D. A. Horner, F. Martín, T. N. Rescigno, and C. W. McCurdy, submitted to PRA (2006).
[30] R. K. Peterkop, Opt. Spectrosc. **13**, 87 (1962).
[31] M. R. H. Rudge and M. J. Seaton, Proc. Roy. Phys. Soc. **283**, 262 (1965).
[32] M. R. H. Rudge, Rev. Mod. Phys. **40**, 564 (1968).
[33] T. N. Rescigno, M. Baertschy, W. A. Isaacs, and C. W. McCurdy, Science **286**, 2417 (1999).
[34] C. W. McCurdy, M. Baertschy, and T. N. Rescigno, J. Phys. B **37**, R137 (2004).
[35] K. E. Banyard, J. Chem. Phys **48**, 2121 (1968).
[36] S. A. Adelman, Phys. Rev. A **5**, 508 (1972).
[37] J. T. Broad and W. P. Reinhardt, Phys. Rev. A **14**, 2159 (1976).
[38] S. Leonardi and C. Calandra, J. Phys. B **26**, L153 (1993).
[39] M. A. Kornberg and J. E. Miraglia, Phys. Rev. A **49**, 5120 (1993).
[40] C. A. Nicolaides, C. Haritos, and T. Mercouris, Phys. Rev. A **55**, 2830 (1997).
[41] K. W. Meyer, C. H. Greene, and B. D. Esry, Phys. Rev. Lett. **78**, 4902 (1997).
[42] A. Kheifets and I. Bray, Phys. Rev. A **58**, 4501 (1998).
[43] M. S. Pindzola and F. Robicheaux, Phys. Rev. A **58**, 4229 (1998).
[44] E. Foumouo, G. L. Katma, G. Edah, and B. Piraux, submitted to Phys. Rev. A (2006).
[45] B. Simon, Phys. Lett. A **71**, 211 (1979).
[46] C. A. Nicolaides and D. R. Beck, Phys. Lett. A **65**, 11 (1978).
[47] C. W. McCurdy and F. Martín, J. Phys. B **37**, 917 (2004).
[48] T. N. Rescigno and C. W. McCurdy, Phys. Rev. A **62**, 032706 (2000).
[49] C. W. McCurdy, D. A. Horner, and T. N. Rescigno, Phys. Rev. A **63**, 022711 (2001).
[50] M. Baertschy, T. N. Rescigno, and C. W. McCurdy, Phys. Rev. A **64**, 022709 (2001).
[51] T. N. Rescigno, M. Baertschy, and C. W. McCurdy, Phys. Rev. A **68**, 020701 (2003).
[52] G. W. F. Drake, in *Atomic, Molecular and Optical Physics Handbook*, edited by G. W. F. Drake and N. E. Hedgecock (AIP, New York, 1996).
[53] M. Foster and J. Colgan, submitted to J. Phys. B (2006).